Identification of constitutive equations at very high strain rates using shock wave produced by laser

Raoudha Seddik, Alexandre Rondepierre, Subramaniyan Prabhakaran, Léo Morin, Véronique Favier, Thierry Palin-Luc, Laurent Berthe

Identification of constitutive equations at very high strain rates using shock wave produced by laser

R. Seddik [a,c,*], A. Rondepierre [a,b], S. Prabhakaran [a], L. Morin [a], V. Favier [a], T. Palin-Luc [c], L. Berthe [a]

[a] Laboratoire PIMM, Arts et Metiers Institute of Technology, CNRS, Cnam, HESAM Universite, 151 Boulevard de l'Hopital, 75013 Paris, France
[b] THALES LAS France, 78990 Elancourt, France
[c] Arts et Metiers Institute of Technology, CNRS, Universite de Bordeaux, Bordeaux INP, I2M Bordeaux, Esplanade des Arts et Metiers 33405 Talence, France

ABSTRACT

A method coupling experiments and simulations, is developed to characterize the yield stress and strain hardening of several metals loaded at 10^6 s^{-1} and < 25 ns, typically involved during Laser Shock Peening. It was applied to four materials: pure aluminum, 2024-T3 and 7175-T7351 aluminum alloys and Ti6Al4V-ELI titanium alloy. Thin foils have been irradiated with high-power laser to induce high-pressure shock wave. Plastic deformation is activated through the thickness up to the rear free-surface of the foils. These experiments have been simulated using three material constitutive equations: Elastic–Perfectly Plastic model considering static yield stress, Johnson–Cook model without strain hardening and Johnson–Cook model with strain hardening. The material parameters of Johnson–Cook law were identified by comparison of the experimental and calculated velocity profiles of the rear-free surface. Results are shown and discussed.

1. Introduction

Laser Shock Peening (LSP) is a surface treatment used in the aerospace industry to improve the fatigue behavior of metallic mechanical components (Clauer, 2012; Zhang et al., 2008; Peyre et al., 1996; Pavan et al., 2019). It consists in impacting the surface of a metallic material, covered with a transparent confinement layer, such as water or quartz, by a high-energy short laser pulses (1–25 J, <25 ns). The instantaneous vaporization of the first microns of the metallic target, caused by irradiation, generates high-pressure plasma (Fabbro et al., 2019). Rapid expansion of such plasma creates a high-pressure shock wave that propagates to the first millimeter in depth of the metal (Anderholm, 1970). The shock wave produces deformation at strain rate higher than 10^6 s^{-1} for short a duration (5–25 ns) (Peyre et al., 1996). When the pressure exceeds the Hugoniot Elastic Limit (HEL) of the metal, the shock wave leads to plastic deformation and compressive residual stress in the material. In addition to residual stresses, strain hardening may be also induced. Nevertheless it is generally limited compared to conventional shot peening (Peyre et al., 1996). This can be explained by the fact that the loading duration is very short and the strain rate is very high, which does not allow the activation of all the sliding systems of the material and thus generates less dislocations. Predicting residual stresses and more generally simulating shock wave propagation at strain rate higher than 10^6 s^{-1} require the use of appropriate constitutive equations. In order to include strain rate sensitivity, various high strain rate dependent formulations have been developed (Zerilli and Armstrong, 1987; Bodner and Partom, 1975; Preston et al., 2003; Ahn and Huh, 2012; Johnson and Cook, 1983; Huh and Khang, 2002; Rule and Jones, 1998; Khan and Huang, 1992; Lee et al., 2006). Zerilli and Armstrong (Zerilli and Armstrong, 1987) proposed a constitutive equation based on the dynamics of dislocations. They accounted for that, for metals with a body-centered-cubic (b.c.c.) crystal structure, the strain rate sensitivity is manifested by an increase in yield stress with strain rate while for face-centered-cubic (f.c.c.) metals, it is related to strain hardening. Thus, they proposed two different models for b.c.c. and f.c.c. metals. In addition, Zerilli and Armstrong's (Zerilli and Armstrong, 1987) model includes the effect of temperature in the term of yield stress for b.c.c. metals and in the term of strain hardening for f.c.c. metals. These constitutive equations were applied and validated with experiments conducted at strain rates up to 10^5 s^{-1}. However, the difficulty in determining the large numbers of material constants makes the implementation of this model very limited. Border and Partom (Bodner and Partom, 1975) developed constitutive equations to model strain rate, temperature and loading

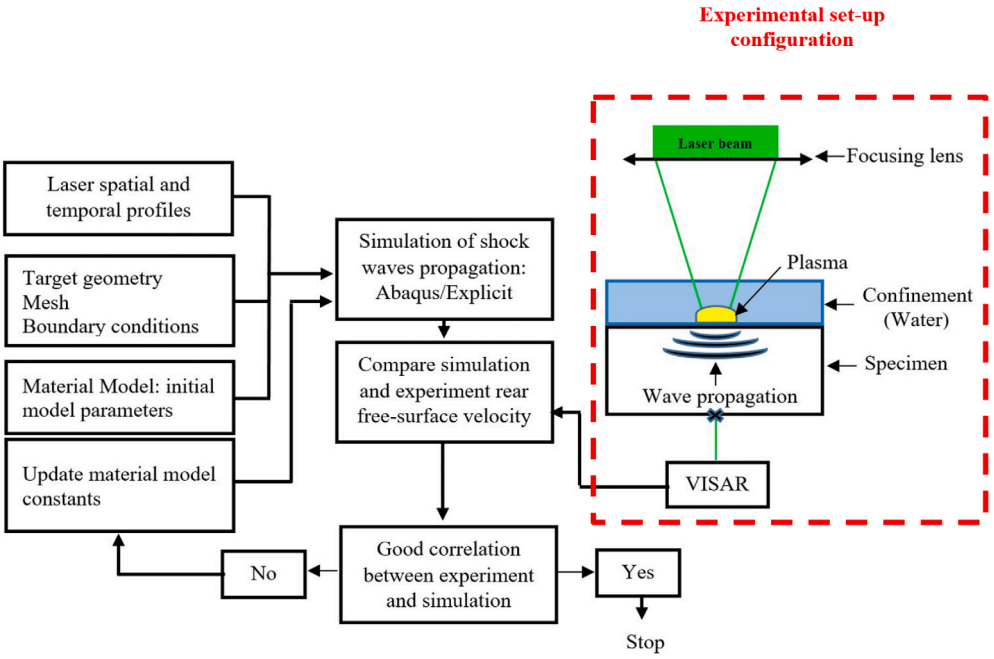

Fig. 1. Flowchart of the proposed methodology.

(unloading) history effects on the mechanical behavior of metals. Their constitutive equations quite successfully reproduced experimental results obtained for aluminum alloys at large finite plastic strain and for strain rate ranging from 10^{-5} s^{-1} to 10^{4} s^{-1} (Khan and Huang, 1992). The numerical implementation of the proposed constitutive equation remains very complex. Preston et al. (2003) suggested two constitutive equations for strain rates up to 10^{5} s^{-1} associated with the so-called thermal regime and for strain rates ranging from 10^{9} s^{-1} to 10^{12} s^{-1} associated with the shock regime, respectively. In the thermal regime, plastic deformation and dislocation velocity are controlled by the dislocation thermally activated overcoming of short range obstacles. In the shock regime, they are controlled by dislocation–phonon drag interactions. The gap between the two regimes is extrapolated. Ahn and Huh (Ahn and Huh, 2012) successfully used the first constitutive equation for f.c.c. copper up to 4×10^{3} s^{-1} but discrepancies between experiments and calculated results exist for b.c.c. steel and h.c.p (hexagonal closest packed) Ti6Al4V alloys. The phenomenological model of Johnson and Cook (1983) is the most commonly used constitutive equation because of the simplicity of its mathematical representation. The number of material parameters is reduced which makes its identification easier. The Johnson–Cook model has been modified by Huh and Khang (2002) and Rule and Jones (1998) in order to provide better description of the mechanical behavior for some materials. The mathematical representation was kept multiplicative. However, the term of strain rate sensitivity was modified. Other modifications of the Johnson–Cook model have been proposed by Khan and Huang (1992) and Lee et al. (2006). For these two modified models the strain hardening term was combined with the strain rate sensitivity one, making more difficult the identification of the material parameters. The Johnson–Cook and modified Johnson–Cook equations were successfully applied for different materials up to 10^{6} s^{-1}. Nevertheless, material parameters need sometimes to be modified with changing temperature and/or strain rate ranges to accurately represent experimental results.

The above discussion reveals that the material parameters of constitutive equations developed for high strain rates have usually been determined by comparison with experimental results obtained for strain rates below 10^{6} s^{-1} which is lower than the strain rates involved in shock waves produced during LSP. It also underlines the interest of "simple" constitutive equation for numerical implementation but also parameter identification. Commonly, the constitutive equation parameters are determined by comparing a calculated stress–strain curve with an experimental one. However under strain rate conditions of 10^{6} s^{-1} and loading times <25 ns, it is no more possible to get such a curve using conventional mechanical testing. When high-pressure loading impacts the front surface of a thin foil, it causes a displacement of the rear free-surface of the target. The velocity of this displacement can be measured by a non-contact method using VISAR (Velocimetry Interferometer System for Any Reflector) Doppler velocimetry. This physical quantity is currently the only directly measurable information during a high-pressure shock wave propagation. It reveals some mechanical characteristics of the material. This technique has been already used to determine the HEL and the yield stress at 10^{6} s^{-1} (Berthe et al., 1997; Hfaiedh et al., 2015).

The objective of the paper is to go further by exploiting all the time profile of the rear free-surface velocity to get information on the material mechanical behavior in the real conditions of high-pressure shock wave characterized by loading duration <25 ns and induced strain rate of about of 10^{6} s^{-1}. An experimental–numerical approach is proposed to obtain the material parameters of constitutive equations. Three "simple" material constitutive models are investigated: elastic–perfectly-plastic model using the yield stress determined thanks to tensile tests in static conditions, the Johnson–Cook law accounting for the strain rate sensitivity of the yield stress but without strain hardening effect and the same with strain hardening effect. The approach is systematically applied to four metals having different static properties such as yield stress: pure aluminum, 2024-T3 aluminum alloy, 7175-T7351 aluminum alloy and Ti-6Al-4V titanium alloy. The paper reports the experimental set-up used to get the rear free-surface velocity during a laser-induced shock wave propagating through thin foils and the finite element model used to simulate the experiments. Results are shown and discussed.

2. Principle of the present methodology

A thin foil of metal is irradiated with a high-intensity laser and a water confinement configuration. The laser–matter interaction produces a high pressure shock wave at the metal target surface which propagates through the thickness of the foil. The laser intensity is chosen to

Table 1
Mechanical properties and foil thickness of studied materials.

Material	ρ (kg/m^3)	ν	E (MPa)	σ_y (MPa)	σ_{yD} (MPa)	P_{HEL} (MPa)	Target thickness (mm)
Pure aluminum	2700	0.33	70 000	90 (Yamada et al., 2018; Hatch, 2005)	164 (Akarca et al., 2008)	320	0.50
2024-T3	2785	0.33	70 000	369 (Ivetic, 2013; Albedah et al., 2017)	340 (Ivetic, 2011)	800	0.50
7075-T7351	2785	0.33	72 000	430 (Zhang et al., 2019)	525 (Zhang et al., 2019)	1030	1.00
Ti6Al4V-ELI	4430	0.33	11 7000	841 (ATI, 2016)	1480 (Ahn and Huh, 2012)	2900	0.38

produce an elastic–plastic shock wave up to the rear free surface of the target. The velocity profile of the rear free surface is measured during all the process using VISAR Doppler velocimetry. Fig. 1 exhibits the set-up configuration. The rear free-surface velocity reveals some mechanical characteristics of the material. A typical profile is given in Fig. 2. The first peak corresponds to the first emergence of the pressure shock. The inflexion corresponds to the elastic–plastic transition under uniaxial shock loading and evidences the so-called elastic precursor as the stress wave separates into two distinct waves: a faster elastic wave and a slower plastic wave. The value of the velocity corresponding to the elastic precursor (V_F) provides the value of the Hugoniot Elastic Limit Pressure P_{HEL} by means of Eq. (1) (Fabbro et al., 1998):

$$P_{HEL} = \frac{1}{2}\rho C_{el} V_F \tag{1}$$

where ρ is the material density, C_{el} is the velocity of the elastic wave given by Eq. (2):

$$C_{el} = \sqrt{\frac{E(1-\nu)}{\rho(1+\nu)(1-2\nu)}} \tag{2}$$

where E is the material Young modulus and ν is the Poisson ratio.

The high-pressure shock wave propagation in the thin foil is also simulated using the commercial finite element code Abaqus. The rear free-surface velocity profile obtained by the experiment and simulation are compared (i) to get information on the mechanical properties in conditions of LSP (with strain rates of about 10^6 s^{-1} and loading duration <25 ns) and (ii) to identify the material parameters of three constitutive equations giving a good match between the experimental and predicted rear free-surface velocity profiles. Providing an elastic–plastic shock wave at the rear free-surface of the thin foil requires that: (i) the maximum pressure is above P_{HEL} and (ii) the thickness of the foil is below the depth affected by the elastic–plastic shock wave. Ballard (1991) developed a model to predict the depth affected by plastic wave (part of the wave which has a pressure above P_{HEL}). This model assumes that (i) the pressure shock wave is longitudinal and produces an uniaxial total deformation along the wave propagation direction, (ii) the pressure pulse is uniform in space and (iii) the material behavior is elastic–perfectly-plastic. For a triangular pulse in time, the plastified depth L is given by Eq. (3):

$$L = \frac{C_{el}C_{pl}\tau}{C_{el}-C_{pl}}\frac{P_{max}-P_{HEL}}{2P_{HEL}} \tag{3}$$

For a square pulse in time, the plastified depth L is given by:

$$L = \frac{C_{el}C_{pl}\tau}{C_{el}-C_{pl}}\frac{P_{max}+P_{HEL}}{2P_{HEL}} \tag{4}$$

where P_{max} is the maximum pressure, τ is the duration of the pulse and C_{pl} is the plastic wave velocity.

The plastic wave velocity is given by Eq. (5):

$$C_{pl} = \sqrt{\frac{E}{3\rho(1-2\nu)}} \tag{5}$$

LSP process is known to produce plastic deformation at depths larger than 1 mm (Peyre and Fabbro, 1995). The maximum plastic deformation is given by Eq. (6):

$$\epsilon_P = \frac{2P_{HEL}(1-2\nu)}{E} \tag{6}$$

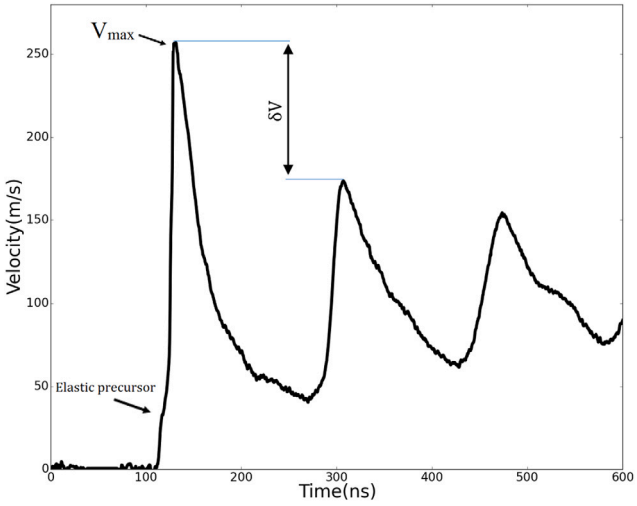

Fig. 2. Rear free-surface velocity typical profile.

In such planar (uniaxial here) deformation state, P_{HEL} is related to the yield stress, σ_{yD}, at the involved strain rate 10^6 s^{-1} by Eq. (7):

$$P_{HEL} = \frac{(1-\nu)}{(1-2\nu)}\sigma_{yD} \tag{7}$$

3. Materials and experimental set-up

3.1. Materials

Four materials have been tested: pure aluminum which is heavily used in automotive and aerospace industries and the properties of which are well-known, the 2024-T3 aluminum alloy which is often used in aircraft structural applications due to its high strength and fatigue resistance, the 7175-T7351 aluminum alloy which is highly utilized by the aerospace industry because it has good resistance to stress corrosion cracking, extruded and annealed Ti6Al4V-ELI titanium alloy which is used in biomedical industry due to its large tensile strength and good biocompatibility. The mechanical properties of these four materials are given in Table 1. The yield stress σ_y were obtained from simple tensile tests in a quasi-static conditions. In addition, the dynamic yield stress at 10^6 s^{-1}, σ_{yD}, found from literature for materials close to the studied ones are also given in Table 1. Literature and studied materials are annealed materials. The dynamic yield stress σ_{yD} were extrapolated from results obtained either to simulate LSP (2024-T3 and 7075-T7351), to simulate machining (pure aluminum) or from slip Hopkinson bar tests (Ti6Al4V). The Hugoniot Elastic Limit Pressure P_{HEL} was deduced from σ_{yD} using Eq. (7). Thin foils of the four studied materials were taken as metal target. Their thickness is given in Table 1. It was chosen between 0.38 mm and 1 mm to be sure that the plastic wave reaches the rear free-surface of the target while to prevent from a too flexible foil.

3.2. Laser and rear free-surface velocity measurement by VISAR

The laser source used to conduct the experiments is the LASER Gaia HP of Hephaistos platform at the PIMM laboratory in Paris. The

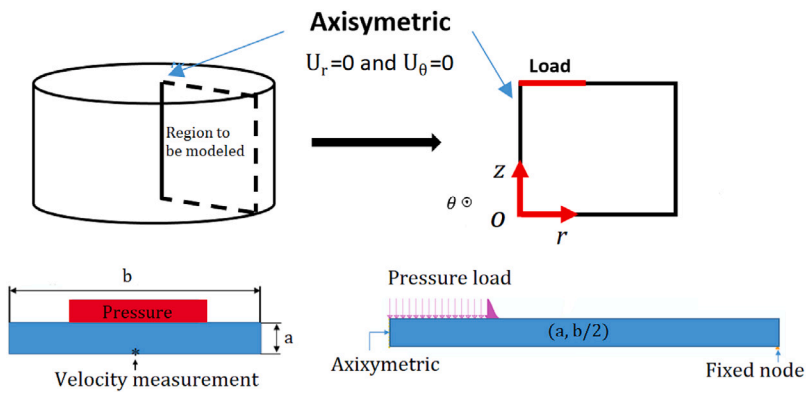

Fig. 3. Geometry and 2D axisymmetric finite element model.

Table 2
Experimental laser process parameters and induced maximum pressure.

Material	Spot diameter (mm)	Intensity (GW/cm^2)	P_{max} (MPa)
Pure aluminum	5	2.25	3000
2024-T3	4	2.97	3100
7175-T7351	5	2.25	3000
Ti6Al4V-ELI	3	6.30	5900

Thales Gaia HP has two separated polarized beams, each one delivers up to 7 Joules at a wavelength of 532 nm. The laser pulse has a temporal profile with a duration of 9 ns at mid-amplitude. As previously explained, the measurement of the rear free-surface velocity is the only available quantitative data revealing the dynamic response of the material under high-pressure shock wave conditions. The investigation of the rear free-surface velocity for the studied materials was performed by using the VISAR Doppler velocimetry that is a non-contact optical acquisition method (Berthe et al., 1997). The PIMM VISAR is based on Barker's system (Barker and Hollenbach, 1972). It is composed of: (i) a continuous laser probe focused on the back surface of a thin target on the center of laser spot, emitting up to 5 W at a wavelength of 532 nm and (ii) an interferometer to create interference fringes from the laser reflected by the back face of the target.

The treatment of interference fringes emitted from interferometer allows direct access to the time profile of the rear free-surface velocity. The intensity of laser beam irradiating the target surface is calculated as the energy divided by the spot area and the pulse duration. It is chosen so that the maximum of the pressure was above P_{HEL}. The maximum pressure was chosen to be above 2000 MPa for aluminum alloys and above 5000 MPa for Ti6Al4V-ELI according to Table 1. Bras et al. (2019) studied the relationship between the laser intensity and the maximum pressure P_{max} for the laser set-up used in this study. Table 2 displays the selected laser intensity and the P_{max} obtained from Bras et al. (2019) study. In addition, Table 2 indicates the chosen spot diameter. Considering laser pulse duration of 9 ns, the laser energy was adjusted to get the right laser intensity. It was selected in order to produce a pressure above the P_{HEL} of the materials but below their critical pressure; above it hydrodynamic effects have to be taken into account. The latter is about 7000 MPa for aluminum alloys and 12 000 MPa for titanium alloys (Ballard, 1991). In such loading pressure conditions the metals behave completely like a solid material and the material response under the high-pressure shock wave only involves its elastic–(visco)-plastic behavior. The process parameters used for the four studied material are given in Table 2.

4. Finite element simulation of high-pressure shock wave propagation

The simulation of shock wave propagation due to a single impact of high pressure at the surface of a thin target has been carried out.

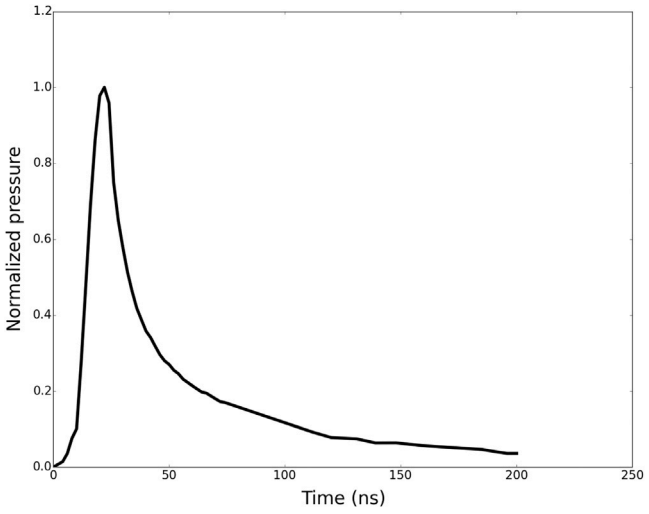

Fig. 4. Time-dependent normalized pressure profile used for the simulation.

The pressure impact is considered as quasi-uniform and axisymmetric in space and very short in time. The whole system (target, loading and boundary conditions) is considered axisymmetric so a 2D axisymmetric model has been developed. Since laser shock process is a high-speed process an explicit solver has been used. The dynamic (inertial and strain rate sensitivity) effects have been considered.

4.1. Geometry and boundary conditions

The target component has been modeled as a plane shell with a thickness, a, ranging from 0.38 mm and 1 mm and a radius $b/2$ of 8 mm (Fig. 3). It was meshed by means of CAX4R elements (Continuum, 4-node bilinear axisymmetric, quadrilateral, reduced integration, hour-glass control). To improve the accuracy of the finite element solutions, a finer mesh has been used in the treated region with the use of a BIAS function in $x-$direction. To investigate mesh size sensitivity, different elements sizes were tested (10 μm × 10 μm, 5 μm × 5 μm, 2 μm × 2 μm and 1 μm × 1 μm). It was checked that as the mesh size decreases, the results became more stable. No difference between the results obtained for 2 μm × 2 μm and 1 μm × 1 μm elements has been observed. Therefore, the treated region was refined with 2 μm × 2 μm elements. For the boundary conditions, one node of the bottom surface has been fixed (Fig. 3). The foils are not clamped in the experiments so a free boundary condition is applied on the right side of the numerical model.

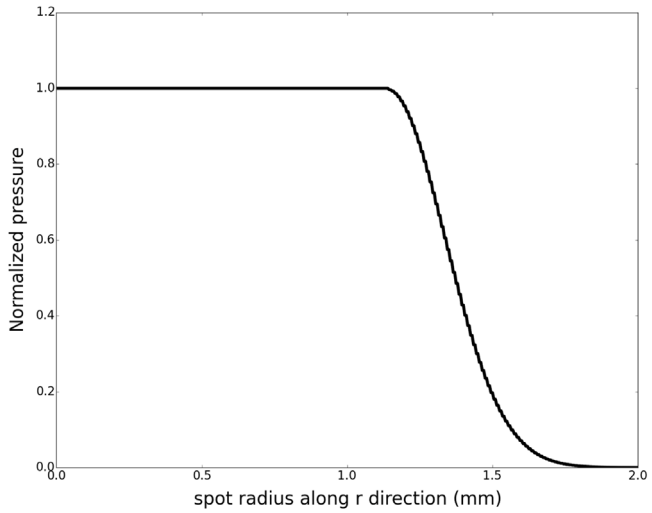

Fig. 5. Radial pressure distribution from the center of the impact: case of a spot diameter = 4 mm.

4.2. Spatial and temporal pressure profiles

To generate spatial and temporal pressure profiles $P = f(r, z, t)$, the Abaqus VDLOAD subroutine was used. Fig. 4 shows the normalized pressure ($P(t)/P_{max}$). P_{max} is given in Table 2. It is worth noting that the duration of the pressure impact (18 ns) is about twice the duration of the laser impact thanks to the plasma confining effects (Peyre et al., 1996). The $P(r, z)$ distribution was obtained from experimental laser beam analysis (see Fig. 5). The intensity profile, obtained through a camera, is used to generate the pressure spatial profile distribution. It defines also the spot diameter. The shape of the temporal pressure profile is closer to triangle than square shape.

4.3. Constitutive model

Three constitutive models were used to simulate the laser-induced shock wave propagation: (i) the elastic–perfectly-plastic (EPP) model considering the static yield stress (ii) the Johnson–Cook (JC) model considering the strain rate sensitivity of the yield stress but without strain hardening and (iii) the Johnson–Cook model with both strain sensitivity and strain hardening. The Johnson–Cook model describes the relationship between strain and stress for metallic components under the conditions of high strain rates, high temperatures and large strains. The isotropic Johnson–Cook model (Johnson and Cook, 1983) is defined by the equivalent Von Mises stress as follows:

$$\sigma = (\sigma_y + K\epsilon_p^n)\left(1 + Cln\left(\frac{\dot{\epsilon_p}}{\dot{\epsilon_{p_0}}}\right)\right)\left(1 - \left(\frac{T - T_0}{T_{melt} - T_0}\right)^m\right) \tag{8}$$

It is composed of three terms in Eq. (8) from left to right: (i) strain hardening, (ii) strain rate sensitivity and (iii) thermal softening.
In Eq. (8), σ_y is the static initial yield stress (annealed material) at room temperature. K and n represent respectively the strain hardening consistency and strain hardening parameter. C is the strain rate sensitivity parameter. T_0 and T_{melt} are room temperature and melting temperature, respectively. $\dot{\epsilon_p}$ is the plastic strain rate and $\dot{\epsilon_{p0}}$ is the reference strain rate. Several studies (Bras et al., 2019; Hfaiedh et al., 2015) have shown that the thermal softening effect has not a significant influence on the laser-induced shock wave through a metallic target. Hence, the thermal softening effect has been neglected in the present study.

Note that at the elastic–plastic transition, $\epsilon_p = 0$ and $\dot{\epsilon_p} = 10^6\ s^{-1}$, the σ_{yD} is given by Eq. (9):

$$\sigma = \sigma_{yD} = \sigma_y\left(1 + Cln(\frac{\dot{\epsilon_p}}{\dot{\epsilon_{p_0}}})\right) \tag{9}$$

The strain hardening rate at a given plastic strain rate and normalized by the Young modulus ($d\sigma/Ed\epsilon$) can be calculated using:

$$\frac{d\sigma}{Ed\epsilon} = Kn\epsilon_p^{(n-1)}\left(1 + Cln(\frac{\dot{\epsilon_p}}{\dot{\epsilon_{p_0}}})\right) \tag{10}$$

First, the laser-induced shock wave was simulated using the elastic–perfectly-plastic constitutive model with the static yield stress, the Young modulus and the Poisson ratio given in Table 1. Secondly, the behavior is assumed to be elastic–perfectly-plastic but characterized by a strain rate sensitive elastic–plastic transition (Johnson–Cook constitutive equation without strain hardening). The identification procedure of other material parameters was performed by comparing qualitatively the calculated and experimental rear free-velocity (magnitude of the velocity and period of the oscillations). The strain rate sensitivity parameter C is used to obtain the same elastic precursor in the rear free-surface velocity profile as experiment. If the obtained rear free-surface velocity profile after the first peak is in good correlation with the experimental one, no other constitutive equation is tested. If not, thirdly, the Johnson–Cook model with strain hardening is used where K and n are identified to get a good match with experiment.

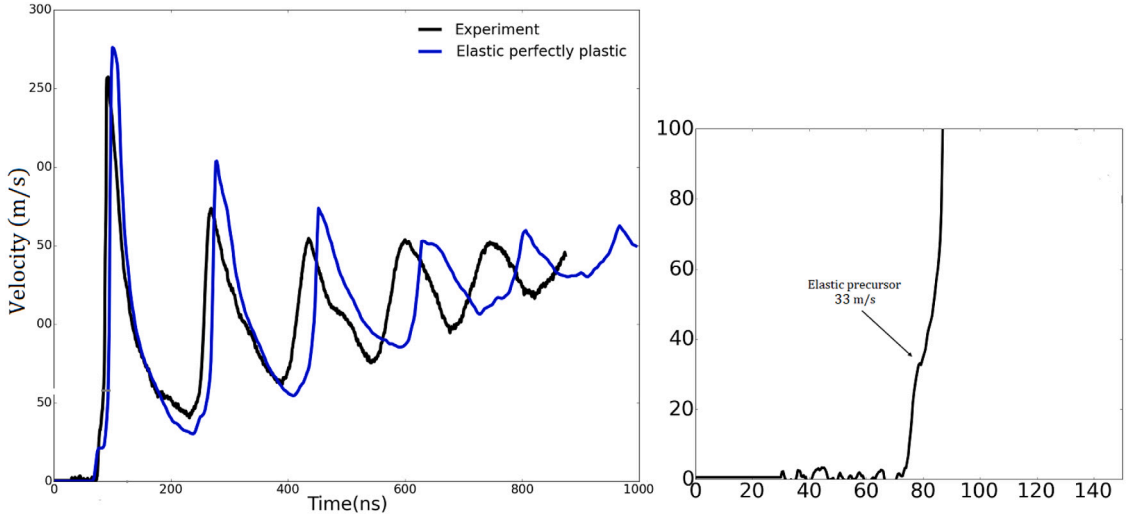

Fig. 6. Calculated and experimental rear free-velocity profiles for pure aluminum using elastic–perfectly-plastic model.

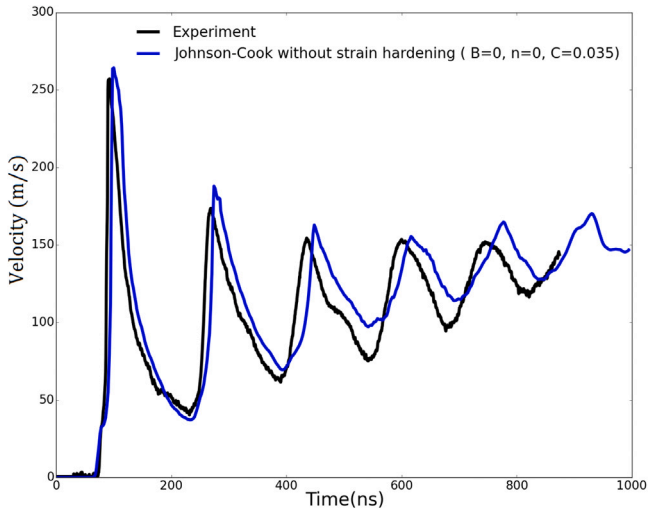

Fig. 7. Calculated and experimental rear free-velocity profiles for pure aluminum using Johnson–Cook without strain hardening model.

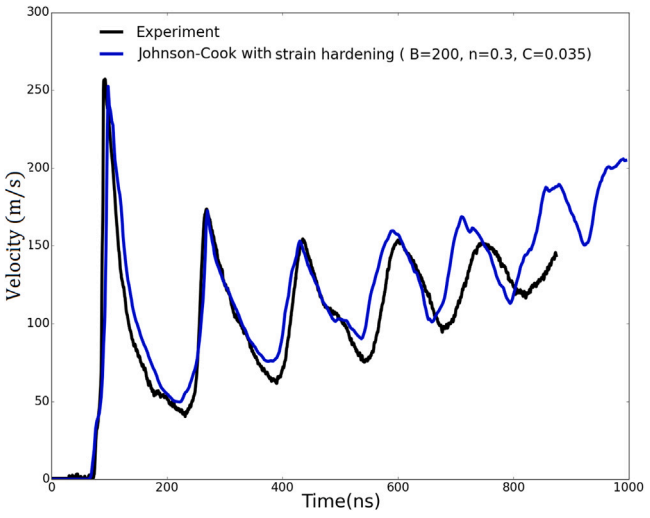

Fig. 8. Calculated and analyzed rear free-velocity profiles for pure aluminum using Johnson–Cook with strain hardening model.

5. Results and discussion

5.1. Present methodology applied to pure aluminum

Figs. 6–8 compare the experimental and simulated rear free-surface velocity profiles in the case of pure aluminum foil. Experimentally, the first peak corresponds to the first emergence of the shock wave. It is followed by secondary shocks occurring at constant period corresponding to the double transit time of the wave through the foil. The magnitude of the rear free-surface velocity at peaks (the decrease in magnitude is noted as δV in Fig. 2) decreases with time and reaches a constant value. This decrease comes from the attenuation of the stress shock wave due to the elastic recoil wave coming back from the surface and reducing the peak pressure at the front surface (Fabbro et al., 1998).

The general trend of this experimental profile is generally well represented by the finite element simulations whatever the chosen constitutive equation. In particular, the maximum value of the rear surface velocity is very well reproduced. The maximum velocity is directly related to the loading pressure. The very good agreement demonstrates that the maximum loading pressure was well estimated from the laser intensity. However, some discrepancies exist which will be discussed in the following subsection.

5.1.1. Prediction of the elastic precursor — identification of strain rate sensitivity parameter

The elastic precursor evidenced by the inflection in the rise of the first peak is experimentally found equal to 33 ms^{-1}. Considering an elastic–perfectly-plastic constitutive equation with a static yield stress results is an underestimation of the elastic precursor 24 ms^{-1} (Fig. 6). This discrepancy was expected as the strain rate sensitivity results in a yield stress at 10^6 s^{-1} higher than the static yield stress and is not taken into account in this simulation. Considering a strain rate sensitivity effect on the yield stress but no strain hardening, the C parameter of the Johnson–Cook law was identified to get a good match between the experimental and calculated elastic precursor. It was found equal to 0.035. Using Eq. (7), we obtained σ_{yD} (10^6 s^{-1}) = 148 MPa. In addition, the P_{HEL} was directly determined form the experimental value of the elastic precursors velocity using Eq. (1). P_{HEL} was found equal to 276 MPa. From Eq. (9), σ_{yD}(10^6 s^{-1}) = 140 MPa. This value is in good agreement with the value deduced from the match of the experimental and simulated velocity profile. This result demonstrates that the experimental rear free-surface velocity profile can be used to straightforwardly determine the P_{HEL}, so a plastic property of a metal in real conditions of LSP. Namely, the laser induced high pressure shock wave through a thin target associated with the analysis of the experimental rear free-surface velocity profile can be considered as a mechanical test.

5.1.2. Prediction of the magnitude and occurrence in time of subsequent peaks of rear surface velocity

A delay in the occurrence of the predicted first peak with regard to the experimental one is observed. It is mostly related to the elastic–plastic transition which is more pronounced in the predicted velocity profile than in the experimental one (Fig. 6). This result is due to the fact that the elastic–perfectly-plastic behavior with a "low" static yield stress does not take into account strain hardening or strain rate effects which could modify the elastic–plastic transition profile (Berthe et al., 1997). Besides, the delay of occurrence of predicted subsequent peaks with regard to the experimental one increases. Additional delay between the first and the third peaks is of 10 ns with regard to the experimental response. When considering the Johnson–Cook law taking into account the dynamic yield stress, the predicted elastic–plastic transition is smoother but the additional delay between the first and third peaks still exists for the simulation (Fig. 7). It vanishes when strain hardening is included in the Johnson–Cook model (Fig. 8). These results suggest that the predicted stress wave velocity is lower for perfect plasticity than for plasticity with strain hardening. Namely, the introduction of strain hardening predicts a higher stress wave velocity that is in good agreement with experimental one. Indeed, the mean stress wave velocity between the first and the third peak was estimated. It is found equal to 5970 ms^{-1} for the experiment. The same value is found for simulation when considering strain hardening while 5800 ms^{-1} is found when considering no hardening. The velocity of the elastic wave is 6200 ms^{-1} (Eq. (2)). The velocity of a plastic wave assuming a perfectly plastic behavior is 5040 ms^{-1} (Eq. (5)). The found value (5970 ms^{-1}) is thus between the velocity of the elastic and perfectly plastic waves. These results demonstrate that pure aluminum exhibits a strain hardening at 10^6 s^{-1} and loading duration <25 ns. The delay of the rear free-surface peak profile can be used to identify the material parameters associated with strain hardening. Note that the increase of plastic wave velocity due to strain hardening is known for a long time (Karman and Duwez, 1950) but was never exploited to identify the strain hardening parameters. Modeling and simulation of high-pressure wave propagation at strain rate higher than 10^6 s^{-1} widely considered elastic–perfectly-plastic behavior accounting for the increase in yield stress due to the high strain rate (Ding and Ye, 2003;

Table 3
Mechanical properties of studied materials.

Material	σ_y (MPa)	K (MPa)	n	C	$\dot{\epsilon_{p0}}$
Pure aluminum	90 (Yamada et al., 2018; Hatch, 2005)	200	0.30	0.035	0.01
2024-T3	369 (Ivetic, 2013; Albedah et al., 2017)	329	0.35	0.025	0.01
7175-T7351	430 (Zhang et al., 2019)	–	–	0.010	0.01
Ti6Al4V-ELI	841 (ATI, 2016)	–	–	0.040	0.01

Table 4
Foil thickness, theoretical plastic length, theoretical and simulated equivalent plastic strain (PEEQ)of studied materials.

Material	Thickness (mm)	L (Ballard, 1991) (triangle pulse, mm)	L (Ballard, 1991) (square pulse, mm)	PEEQ saturated	PEEQ from Ballard's model (Ballard, 1991)
Pure aluminum	0.50	2.3	2.8	2.0×10^{-3}	2.7×10^{-3}
2024-T3	0.50	0.5	1.0	6.3×10^{-3}	10.0×10^{-3}
7175-T7351	1.00	0.5	1.0	3.8×10^{-3}	10.0×10^{-3}
Ti6Al4V-ELI	0.38	0.3	0.7	3.5×10^{-3}	16.9×10^{-3}

Hu et al., 2006). Isotropic strain hardening through the Johnson–Cook was also used (Peyre et al., 2003; Ivetic, 2011; Hfaiedh et al., 2015; Zhang et al., 2019). However, the criterion to choose the parameters K and n is not indicated. Table 3 gives the C, K and n values for the studied materials.

Table 4 shows the plastified depth L determined from Eqs. (4) and (5) considering P_{max}, P_{HEL} and τ from experiments. As expected, L is larger than the thin foil thickness chosen to provide plastic strain at the rear free-surface. The predicted equivalent plastic deformation using Abaqus simulation reaches 74% of the maximum plastic deformation predicted by Ballard's model. It is found equal to 2×10^{-3}. Which is quite small. Consequently, the strain hardening parameters are identified in plastic strain conditions much smaller than those commonly used in quasi-static mechanical tests, involving plastic strain typically ranging from 2×10^{-3} to 0.3. The comparison of strain hardening obtained here with the static one requires to investigate the same plastic strain range ($< 2 \times 10^{-3}$). Identified strain hardening parameters provide ($d\sigma/Ed\epsilon$) at 10^6 s^{-1} and $< 2 \times 10^{-3}$ plastic strain equal to 0.11. This value is similar to the one estimated from tensile stress–strain curves carried out in monotonic quasi-static conditions (Yamada et al., 2018; Sahu et al., 2018). Consequently, the present methodology shows that for pure aluminum, the strain hardening rate is not significantly changed with increasing strain rate for plastic strain $\leqslant 2 \times 10^{-3}$.

5.2. Application to 2024-T3, 7175-T7351 and Ti6Al4V-ELI

Fig. 9 depicts the rear free-surface velocity variation, experiment and simulation, versus time using the elastic–perfectly-plastic, Johnson–Cook without strain hardening and Johnson–Cook with strain hardening constitutive equations for the 2024-T3 aluminum alloy material.

As for pure aluminum, the general experimental trends, occurrence time and magnitude of peaks in rear free-surface velocity, as quite well reproduced by the simulations whatever the constitutive models. However, it is clearly noticeable that the elastic–perfectly-plastic constitutive equation with static yield stress very underestimates the elastic precursor. Indeed, the calculated elastic precursor is 85 ms^{-1} and the measured one is 121 ms^{-1}. It is also noted, that the predicted elastic precursor is more pronounced as for the pure aluminum case, leading to a delay between the experimental and predicted peaks of 9 ns. In addition, the predicted rear free-surface second and third peaks occur with an additional slight delay with regard to the experimental ones. The additional delay of occurrence of the third peak is equal to 30 ns. From these results, we can conclude that the 2024-T3 aluminum alloy behavior is strain rate sensitive and exhibits strain hardening at 10^6 s^{-1}. Following the present methodology, the C parameter of the Johnson–Cook law was estimated to 0.025 to match the experimental and calculated elastic precursor. P_{HEL} and the dynamic yield stress at 10^6 s^{-1} were found equal to 1028 MPa and 539 MPa, respectively, which are in very good agreement with Hfaiedh et al. (2015). A direct identification of σ_{yD} from V_f, Eqs. (1) and (2), results in $\sigma_{yD} = 522$ MPa that is in good agreement with 539 MPa. Taking into account dynamic yield stress at 10^6 s^{-1} provides a good representation of the elastic precursor as expected and reduces the delay between experimental and calculated peaks. The K and n parameters associated with strain hardening were adjusted in order to reduce the delay between the experimental and calculated peaks. They were found equal to $K =$ 392 MPa and $n = 0.35$.

The predicted equivalent plastic strain using Abaqus simulation reaches 63% of the maximum plastic strain estimated from Ballard's model and is predicted equal to 6.3×10^{-3}. Taking into account this value, the strain hardening rate normalized by the Young Modulus is found equal to 0.06 at 10^6 s^{-1}. It is similar to the one obtained at 10^5 s^{-1} by Daoud et al. (2015), 0.05 and higher than 0.03, the value estimated from a quasi-static monotonic tensile stress–strain curve (Albedah et al., 2017). These comparisons suggest that the strain hardening rate for plastic strain $\leqslant 6 \times 10^{-3}$ slightly increases with increasing strain rate.

Figs. 10 and 11 illustrate a comparison between the rear free-velocity profiles measured with VISAR and the values obtained by simulations for 7175-T7351 aluminum alloy and the Ti6Al4V-ELI, respectively.

The elastic–perfectly-plastic model considering static yield stress underestimates the elastic precursor and leads to a too pronounced elastic–plastic transition for both materials leading to a delay of occurrence for the first peaks. For the 7175-T7351 aluminum alloy, the predicted elastic precursor is 92 ms^{-1} and the measured is 107 ms^{-1}. For Ti6Al4V-ELI, the calculated and the measured elastic precursors are 120 ms^{-1} and 210 ms^{-1}, respectively. The C parameter was adjusted to successfully represent the elastic precursor and was found equal to 0.01 and 0.04, respectively for 7175-T7351 alloy and Ti6Al4V-ELI. The C value for 7175-T7351 alloy is the same as the C parameter used in Zhang et al. (2019). It provides a P_{HEL} and a dynamic yield stress at 10^6 s^{-1} of 920 MPa and 500 MPa, respectively. For Ti6AlV4-ELI the P_{HEL} and dynamic yield stress at 10^6 s^{-1} were found equal to 2900 MPa and 1460 MPa, respectively. As far as the other peaks are concerned, interestingly, no significant additional delay between the occurrence of the experimental and predicted peaks was measured. For both materials, results indicate that the Johnson–Cook model without strain hardening has good agreement with experimental results. These results show that strain hardening was not involved in the experiments. Table 4 compares the thickness of the studied foils and the length of the plastic affected zone according to Ballard's model (Ballard, 1991) considering an triangle or square pulse in time. The thickness of 7075-T7351 and Ti6Al4V-ELI are below or close to the theoretical plastic affected length. The presence of elastic precursor in Figs. 10 and 11 confirms the onset of plastic strain but its magnitude is probably too low to evidence strain hardening.

Indeed, the predicted equivalent plastic strain at the rear free-surface is 44% and 21% of the maximum possible plastic strain predicted by Ballard's model (Table 4). The mean shock wave velocity

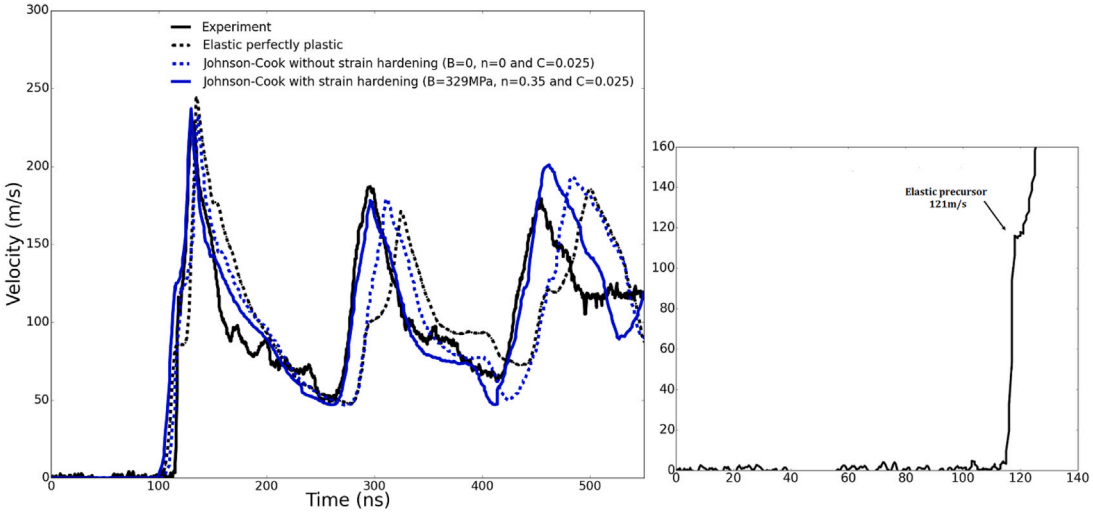

Fig. 9. Calculated and experimental rear free-velocity profiles for 2024-T3 aluminum alloy using three different constitutive models.

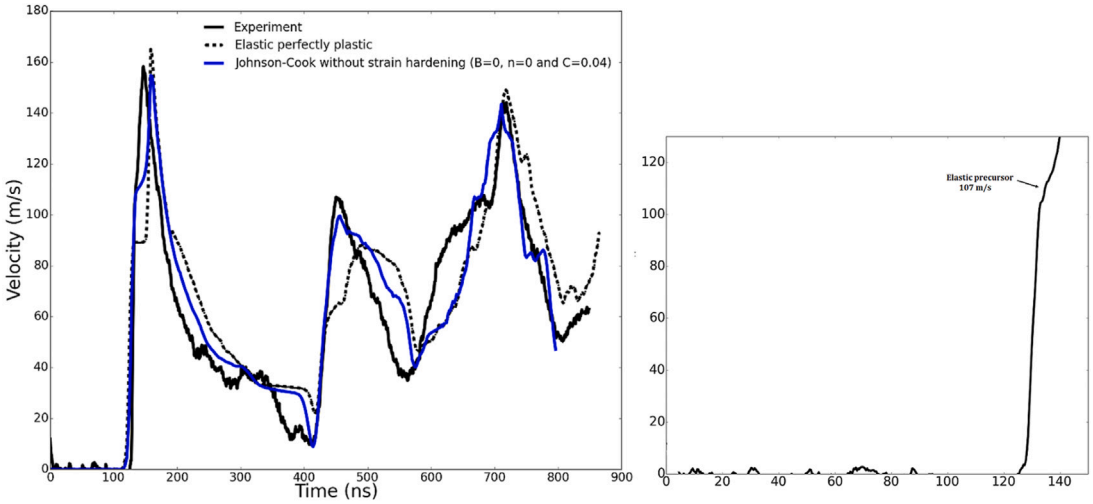

Fig. 10. Calculated and experimental rear free-velocity profiles for 7175-T7351 aluminum alloy using three different constitutive models.

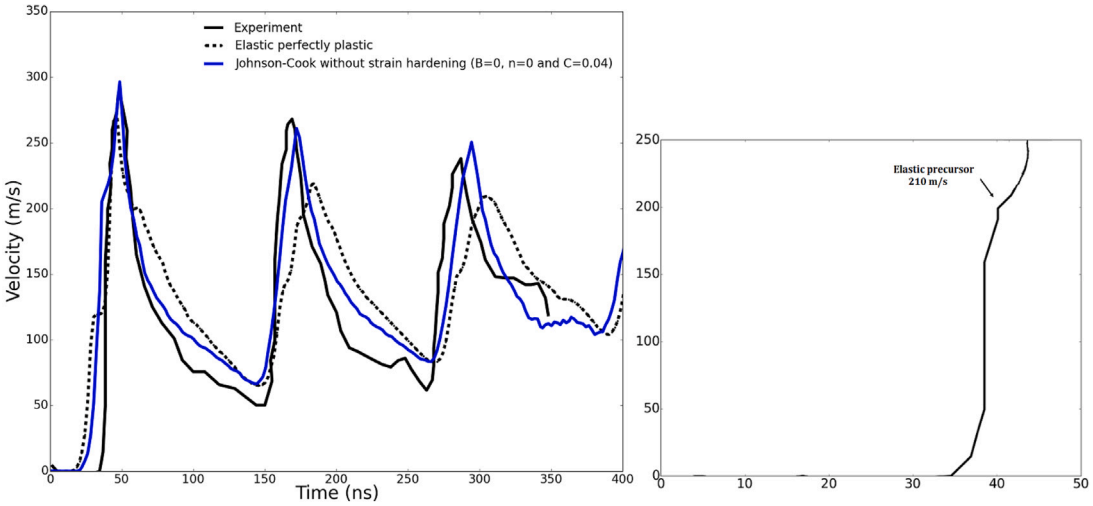

Fig. 11. Calculated and experimental rear free-velocity profiles for Ti6Al4V-ELI titanium alloy using three different constitutive models.

estimated from the experimental first and third peaks is equal to 6667 ms^{-1} for 7175-T7351 alloy and 6307 ms^{-1} for Ti6Al4V-ELI. These values are close to the velocity of the elastic wave (6190 ms^{-1} for 7175-T7351 alloy and 6255 ms^{-1} for Ti6Al4V-ELI). The fact that the values are even above the elastic wave velocity is due to the uncertainty in Young Modulus usually estimated with tensile tests while compression state involves during laser-induced shock wave. The maximum compressive Young modulus of Ti6Al4V-ELI is 124 000 MPa. This value provides an elastic wave velocity equal to 6440 ms^{-1}. This comparison reveals that the stress shock wave propagates mainly in an elastic medium.

All these results show that the analysis of the rear free surface velocity peaks subsequent to the first peak gives useful information on the strain-hardening of the material loaded at 10^6 s^{-1} and during less than 25 ns. It allows the identification of strain-hardening parameters of constitutive equations. Nevertheless, this requires experimental conditions promoting enough plastic deformation (at least above 44% of the maximum possible plastic strain determined by Ballard's model (Ballard, 1991))

6. Conclusion

A method coupling experiments and modeling is proposed to identify the parameters of three constitutive equations in the case of strain rate around 10^6 s^{-1} and for test duration below 25 ns (LSP conditions). It is shown that:

1. A laser induced high-pressure loading impact on the front surface of a thin metal target can be used as a mechanical test to investigate strain rate sensitivity and strain hardening of the material. The experimental data used is the rear free-surface velocity time profile of the target.
2. The strain rate sensitive parameter of the Johnson–Cook constitutive equation is determined from the elastic precursor (in the rise of the first peak of the velocity profile).
3. The yield stress at 10^6 s^{-1} was found equal to 1.6 times the quasi-static yield stress for pure aluminum, 1.4 for 2024-T3, 1.1 for 7175-T7351 and 1.7 for Ti6Al4V-ELI.
4. The strain hardening parameters can be identified using the delay between the first peak and the second/third peaks.
5. Characterizing strain hardening requires experimental conditions promoting plastic strain at the rear free-surface at least higher than 44% of the maximum possible plastic strain determined by Ballard's model. In these experiments, the plastic strain involved is approximately values of few 10^{-3} have been found for plastic strain at the rear free-surface.

CRediT authorship contribution statement

R. Seddik: Conceptualization, Methodology, Software, Writing - Original Draft. **A. Rondepierre:** Investigation, Methodology. **S. Prabhakaran:** Investigation, Methodology. **L. Morin:** Software, Writing - Review & Editing, Supervision. **V. Favier:** Conceptualization, Writing - Review & Editing, Supervision. **T. Palin-Luc:** Conceptualization, Writing - Review & Editing, Supervision. **L. Berthe:** Conceptualization, Writing - Review & Editing, Supervision, Project administration.

Declaration of competing interest

The authors declare that they have no known competing financial interests or personal relationships that could have appeared to influence the work reported in this paper.

References

Ahn, K., Huh, H., 2012. Comparison of dynamic hardening equations for metallic materials with three types of crystalline structures. In: 5th International Conference on High Speed Forming.

Akarca, S., Song, X., Altenhof, W.J., Alpas, A.T., 2008. Deformation behaviour of aluminium during machining: Modelling by Eulerian and smoothed-particle hydrodynamics methods. Proc. Inst. Mech. Eng. L 222 (3), 209–221.

Albedah, A., Khan, S.M.A., Bouiadjra, B., Benyahia, F., 2017. Fatigue crack propagation in aluminum plates with composite patch including plasticity effect. Proc. Inst. Mech. Eng. G 232, 2122–2131.

Anderholm, N., 1970. Laser-generated stress waves. Appl. Phys. Lett. 16, 113–115.

ATI, 2016. Specialty Alloys and Components, Franckville Operations:Doc 37246. Product certification, pp. 1–3.

Ballard, P., 1991. Contraintes Résiduelles Induites Par Impact Rapide. Application au Choc Laser (Ph.D. thesis). Ecole polytechnique.

Barker, L.M., Hollenbach, R.E., 1972. Laser interferometer for measuring high velocities of any reflecting surface. J. Appl. Phys. 43 (11), 4669–4675.

Berthe, L., Fabbro, R., Peyre, P., Tollier, L., Bartnicki, E., 1997. Shock waves from a water-confined laser-generated plasma. Mater. Sci. Eng. 82, 2826–2832.

Bodner, S.R., Partom, Y., 1975. Constitutive equations for elastic-viscoplastic strain hardening materials. J. Appl. Mech. 42, 385–389.

Bras, C. Le, Rondepierre, A., Seddik, R., Scius-Bertrand, M., Rouchausse, Y., Videau, L., Fayolle, B., Gervais, M., Morin, L., Valadon, S., Ecault, R., Furfari, D., Berthe, L., 2019. Laser shock peening: Toward the use of pliable solid polymers for confinement. Metals 9, 793–806.

Clauer, A.H., 2012. Surface Performance of Titanium:Laser Shock Peening for Fatigue Resistance. Woodhead Publishing.

Daoud, M., Chatelain, J.F., Bouzid, A., 2015. Effect of rake angle on Johnson-Cook material constants and their impact on cutting process parameters of Al2024-T3 alloy machining simulation. Int. J. Adv. Manuf. Technol. 81, 1987–1997.

Ding, K., Ye, L., 2003. Three-dimensional dynamic finite element analysis of multiple laser shock peening processes. Surf. Eng. 19, 351–358.

Fabbro, R., Fournier, J., Ballard, P., Devaux, D., Virmont, J., 2019. Physical study of laser-produced plasma in confined geometry. J. Appl. Phys. 68, 775–784.

Fabbro, R., Peyre, P., Berthe, L., 1998. Physics and applications of laser shock processing. J. Laser Appl. 10, 265–279.

Hatch, J.E., 2005. Aluminum: Properties and Physical Metallurgy. American society for metals, pp. 1–24.

Hfaiedh, N., Peyre, P., Song, H., Popa, I., Ji, V., Vignal, V., 2015. Finite element analysis of laser shock peening of 2050-T8 aluminum alloy. J. Manuf. Sci. Eng. Trans. ASME 70, 480–489.

Hu, Y., Yao, Z., Hu, J., 2006. 3D FEM simulation of laser shock processing. Surf. Coat. Technol. 201, 1426–1435.

Huh, H., Khang, W.J., 2002. Crash worthiness assessment of thin wall structure with the high strength steel sheet. Int. J. Veh. Des. 30, 1–21.

Ivetic, G., 2011. Three-dimensional FEM analysis of laser shock peening of aluminium alloy 2024-T351 thin sheets. Surf. Eng. 27 (6), 445–453.

Ivetic, G., 2013. Three-dimensional FEM analysis of laser shock peening of aluminium alloy 2024-T351 thin sheets. Opt. Laser Technol. 111, 445–453.

Johnson, G., Cook, W.H., 1983. A constitutive model and data for materials subjected to large strains, high strain rates, and high temperatures. In: Proceedings of the 7th International Symposium on Ballistics. The Netherlands, pp. 541–547.

Karman, T. Von, Duwez, P., 1950. The propagation of plastic deformation in solids. J. Appl. Phys. 21, 987–994.

Khan, A.S., Huang, S., 1992. Experimental and theoretical study of mechanical behavior of 1100 aluminum in the strain rate range $10^4 s^{-1}$ - $10^5 s^{-1}$. Int. J. Plast. 8 (4), 397–424.

Lee, H.J., Song, J.H., Huh, H., 2006. Dynamic tensile tests of auto-body steel sheets with the variation of temperature. Solid State Phenom. 116–117, 259–262.

Pavan, M., Furfari, D., Ahmad, B., Gharghouri, M., Fitzpatrick, M., 2019. Laser shock processing of aluminium alloys:application to high cycle fatigue behaviour. Int. J. Fatigue 123, 157–167.

Peyre, P., Fabbro, R., 1995. Laser shock processing: A review of the physics and applications. Optim. Quant. Electron. 27, 1213–1229.

Peyre, P., Fabbro, R., Merrien, P., Lieurade, H.P., 1996. Laser shock processing of aluminium alloys: Application to high cycle fatigue behaviour. Mater. Sci. Eng. A 210, 102–113.

Peyre, P., Sollier, A., Chaieb, I., Berthe, L., Bartnicki, E., Braham, C., Fabbro, R., 2003. FEM simulation of residual stresses induced by laser Peening. Appl. Phys. 23, 83–88.

Preston, D.L., Tonks, D.L., Wallace, D.C., 2003. Model of plastic deformation for extreme loading conditions. J. Appl. Phys. 93, 211–220.

Rule, W.K., Jones, S.E., 1998. A revised form for the Johnson-Cook strength model. Int. J. Impact Eng. 21, 609–624.

Sahu, S., Mondal, D.P., Goel, M.D., Ansari, M.Z., 2018. Finite element analysis of AA1100 elasto-plastic behaviour using Johnson-Cook model. Mater. Today: Proc. 5, 5349–5353.

Yamada, H., Kami, T., Mori, R., Kudo, T., Okada, M., 2018. Strain rate dependence of material strength in AA5xxx series aluminum alloys and evaluation of their constitutive equation. Metals 8, 576–590.

Zerilli, F.J., Armstrong, R.W., 1987. Dislocation-mechanics-based constitutive relations for material dynamics calculations. J. Appl. Phys. 61 (5), 1816–1825.

Zhang, X., Huang, Z., Chen, B., Zhang, Y., Tong, J., Fang, G., Duan, S., 2019. Investigation on residual stress distribution in thin plate subjected to two sided laser shock processing. Opt. Laser Technol. 111, 146–155.

Zhang, Y., Lu, J., Ren, X., Yao, H., 2008. Effect of laser shock processing on the mechanical properties and fatigue lives of the turbojet engine blades manufacture by YL2 aluminum alloy. Mater. Des. 30, 1697–1703.